

# A novel computational approach for wind-driven flows over deformable topography

Alia Al-Ghosoun<sup>1</sup> and Mohammed Seaid<sup>2</sup>

<sup>1</sup> Mechatronics engineering department, Philadelphia University, Amman, Jordan,  
aalghsoun@philadelphia.edu.jo

<sup>2</sup> Department of Engineering, Durham university, South Road, Durham, DH13LE,  
United Kingdom, m.seaid@durham.ac.uk

**Abstract.** Single-layer shallow water models have been widely used for simulating shallow water waves over both fixed and movable beds. However, these models can not capture some hydraulic features such as small eddy currents and flow recirculations. This study presents a novel numerical approach for coupling multi-layer shallow water models with elastic deformations to accurately capture complex recirculation patterns in wind-driven flows. This class of multi-layer equations avoids the computationally demanding methods needed to solve the three-dimensional Navier-Stokes equations for free-surface flows while it provides stratified flow velocities since the pressure distribution is still assumed to be hydrostatic. In the current study, the free-surface flow problem is approximated as a layered system made of multiple shallow water equations of different water heights but coupled through mass-exchange terms between the embedded layers. Deformations in the topography are accounted for using linear elastostatic systems for which an internal force is applied. Transfer conditions at the interface between the water surface and the topography are also developed using frictional forces and hydrostatic pressures. For the computational solver, we implement a fast and accurate hybrid finite element/finite volume method solving the linear deformations on unstructured meshes and the nonlinear flows using well-balanced discretizations. Numerical results are presented for various problems and the computed solutions demonstrate the ability of the proposed model in accurately resolving wind-driven flows over deformable topography.

**Keywords:** Multi-layer shallow water · Elasticity · Finite volume method · Finite element method · Topography deformation · Wind-driven flows.

## 1 Introduction

Free-surface models in hydraulic applications have gained an increasing interest during the last decades, see for example [13]. Ranging from flood forecasting [20] to monitoring hydraulic infrastructures such as dams and rivers [22]. Water free-surface flows under the influence of gravity can be modelled using the well-established shallow water equations [3]. However, the main drawback of these equations lies in the lack of capturing some crucial physical dynamics in the

vertical motion of water flow [1]. Moreover, under the impact of topography and wind forces, the hydrodynamics can be very complex and numerical modelling of such problems would require the use of the full three-dimensional Navier-Stokes equations [6]. Recently, multi-layer shallow water models have attracted enormous attention and become an important tool to capture many hydraulic problems such as the flow recirculations [4]. The multi-layer shallow water equations have also been subject of various research studies and have been used for modelling a wide variety of free-surface flows where water flows interact with the bed topography [21] and wind stresses [5]. For example, researchers in [12] have implemented the multi-layer model to study nonlinear internal wave propagation in shallow water flows, whereas in [10], authors have experimentally investigated the multi-layer flow field mapping in a small scale shallow water reservoir by coastal acoustic tomography. On the other hand, the incompressible smoothed particle hydrodynamics approach has been implemented in [14] to model dam-break flows over movable beds.

Different numerical methods were implemented in the literature to model the multi-layer shallow water flows. In [22], the finite difference method is used to solve a multi-layer model with non-flat bottom topography on both fixed and adaptive moving meshes [8]. A well-balanced Runge-Kutta discontinuous Galerkin method has also been proposed in [11] for the numerical solution of multi-layer shallow water equations with mass exchange and non-flat bottom topography. In recent years, a great amount of research effort has been devoted to developing consistent mathematical models and efficient numerical solvers for the interaction between topography deformation and water waves. In practice, modelling of wave flows by static deformation is based on two components including the description of topography deformation and the governing equations of the water flow. In [18, 1], we have used the conventional single-layer shallow water equations for modelling flows over deformable beds. These models performed very well for simple flows such as dam-break and stream-flow problems as well as water waves generated by deformations on the topography. However, these models would fail to adequately represent flow circulations and do not account for the influences of wind effect and water layer densities in their formulations. Therefore, the present study is an improvement to our previous research in [1, 18] using the multi-layer shallow water equations. In this work, the governing equations consist of the one-dimensional nonlinear multi-layer shallow water equations for the water flow and a two-dimensional linear elastostatic model for the deformation of topography. In addition to the internal stress applied to the bed, deformations in the topography can also be caused as a result of the hydrostatic pressure distribution and the frictional force obtained from the shallow water flow. These equations are fully coupled and solved simultaneously in time using transfer conditions at the interface between the water flow and the topography. This allows for hydrostatic pressure and friction forces to be implemented for the elastostatic equations whereas the deformed topography is accounted for in the multi-layer shallow water equations through the bathymetric forces. To solve the considered system we implement a well-balanced finite

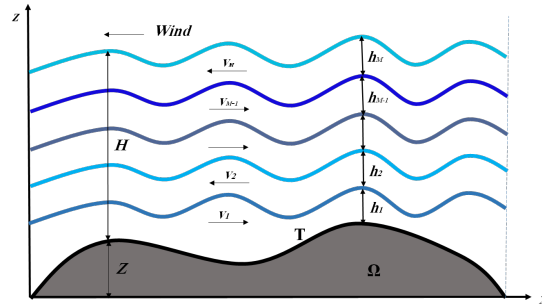


Fig. 1: Illustration of a coupled system for wind-driven flows over deformable topography.

volume method for the multi-layer shallow water system and a stabilized finite element method for linear elasticity equations. This hybrid finite element/finite volume solver uses unstructured/structured meshes, respectively. The interfacial forces are sampled from the hydrostatic pressure and applied on the topography to be used in the stress analysis. To demonstrate the performance of the hybrid finite volume/finite element method, computational results obtained for wind-driven flows over deformable topography are presented. The effects of wind velocity, number of layers on the flow field and stress distributions are also investigated in this study. The rest of this paper is organized as follows: Formulation of mathematical models for the coupled system is presented in section 2. Section 3 is devoted to the implementation of the numerical methods used for the solution procedure. Numerical results and examples for wind-driven flows over deformable topography are presented in section 4. Concluding remarks are summarized in section 5.

## 2 Governing equations for wind-driven flows over deformable topography

Considering the system illustrated in Figure 1, the proposed coupled system consists of the two-dimensional constitutive relations of an isotropic elastic bed and the multi-layer shallow water equations. In elasticity theory [9], the bed deformation equations can be written as a relationship between the stress and strain in terms of the Lamé parameters as

$$\nabla \cdot \boldsymbol{\sigma} = \mathbf{f}, \quad \boldsymbol{\sigma} = \lambda \text{tr}(\boldsymbol{\epsilon}) \mathbf{I} + 2\mu \boldsymbol{\epsilon}, \quad (1)$$

where  $\boldsymbol{\sigma}$  is the stress tensor,  $\mathbf{f}$  the body force per unit area,  $\lambda$  the first Lamé parameter (related to the bulk modulus),  $\text{tr}(\boldsymbol{\epsilon})$  the trace of the strain tensor,  $\mathbf{I}$  the identity matrix,  $\mu$  the second Lamé parameter (related to the shear modulus). The displacement vector is denoted by  $\mathbf{u} = (u_x, u_z)^\top$  and  $\boldsymbol{\epsilon}$  the infinitesimal strain

tensor defined by

$$\boldsymbol{\epsilon} = \frac{1}{2} \left( \nabla \mathbf{u} + (\nabla \mathbf{u})^\top \right). \quad (2)$$

Combining equations (1) and (2), one obtains

$$\boldsymbol{\sigma} = \lambda (\nabla \cdot \mathbf{u}) \mathbf{I} + \mu (\nabla \mathbf{u} + (\nabla \mathbf{u})^\top). \quad (3)$$

The system is equipped with the following boundary conditions

$$\boldsymbol{\sigma} = \boldsymbol{\sigma}_c, \quad \mathbf{u} = \mathbf{0}, \quad \text{on } \partial\Omega, \quad (4)$$

where  $\partial\Omega$  is the fixed boundary of the topography domain  $\Omega$  and  $\boldsymbol{\sigma}_c$  is a prescribed stress. In the current study, the constitutive relation is defined as

$$\boldsymbol{\sigma} = \mathbf{D} \boldsymbol{\epsilon}, \quad (5)$$

where the stress vector  $\boldsymbol{\sigma}$  and the constitutive matrix  $\mathbf{D}$  for a plane-strain case are given as

$$\boldsymbol{\sigma} = \begin{pmatrix} \sigma_x \\ \sigma_z \\ \tau_{xz} \end{pmatrix}, \quad \mathbf{D} = \frac{E}{(1+\nu)(1-2\nu)} \begin{pmatrix} 1-\nu & \nu & 0 \\ \nu & 1-\nu & 0 \\ 0 & 0 & \frac{1-2\nu}{2} \end{pmatrix},$$

with  $E$  is the Young's modulus characterising the bed material and  $\nu$  the Poisson's ratio, the two Lamé parameters are given as

$$\lambda = \frac{E\nu}{(1+\nu)(1-2\nu)}, \quad \mu = \frac{E}{2(1+\nu)}.$$

For the wind-driven flows, we assume  $M$  layers of water bodies bounded at the bottom by the deformable topography and a free-surface subjected to wind stresses as illustrated in Figure 1. For simplicity in the presentation, the governing equations for the multi-layer shallow water model considered in the present work read as

$$\frac{\partial \mathbf{W}}{\partial t} + \frac{\partial \mathbf{F}(\mathbf{W})}{\partial x} = \mathbf{Q}(\mathbf{W}) + \mathbf{R}(\mathbf{W}), \quad (6)$$

where  $\mathbf{W}$  is the vector of conserved variables,  $\mathbf{F}$  the vector of flux functions,  $\mathbf{Q}$  and  $\mathbf{R}$  are the vectors of source terms defined by

$$\mathbf{W} = \begin{pmatrix} H \\ H v_1 \\ H v_2 \\ \vdots \\ H v_M \end{pmatrix}, \quad \mathbf{F}(\mathbf{W}) = \begin{pmatrix} \sum_{\alpha=1}^M l_\alpha H v_\alpha \\ H v_1^2 + \frac{1}{2} g H^2 \\ H v_2^2 + \frac{1}{2} g H^2 \\ \vdots \\ H v_M^2 + \frac{1}{2} g H^2 \end{pmatrix}, \quad \mathbf{Q}(\mathbf{W}) = \begin{pmatrix} 0 \\ -g H \frac{\partial Z}{\partial x} \\ -g H \frac{\partial Z}{\partial x} \\ \vdots \\ -g H \frac{\partial Z}{\partial x} \end{pmatrix},$$

$$\mathbf{R}(\mathbf{W}) = \begin{pmatrix} 0 \\ \frac{1}{l_1} \left( \mathcal{S}_1 - gn_b^2 \frac{v_1 |v_1|}{H^{1/3}} + 2\xi \frac{v_2 - v_1}{(l_2 + l_1) H} \right) \\ \frac{1}{l_2} \left( \mathcal{S}_2 + 2\xi \frac{v_3 - v_2}{(l_3 + l_2) H} - 2\xi \frac{v_2 - v_1}{(l_2 + l_1) H} \right) \\ \vdots \\ \frac{1}{l_{M-1}} \left( \mathcal{S}_{M-1} + 2\xi \frac{v_M - v_{M-1}}{(l_M + l_{M-1}) H} - 2\xi \frac{v_{M-1} - v_{M-2}}{(l_{M-1} + l_{M-2}) H} \right) \\ \frac{1}{l_M} \left( \mathcal{S}_M - \sigma^2 \rho_a \frac{w |w|}{H} - 2\xi \frac{v_M - v_{M-1}}{(l_M + l_{M-1}) H} \right) \end{pmatrix}. \quad (7)$$

where,  $v_\alpha(t, x)$  is the local water velocity for the  $\alpha$ th layer,  $Z(x)$  the bed topography,  $g$  the gravitational acceleration,  $H(t, x)$  the water height of the whole flow system, we refer the reader to [11] for the more details. In (7), the source term  $\mathcal{S}_\alpha$  represents the momentum exchanges between the water layers defined as

$$\mathcal{S}_\alpha = u_{\alpha+\frac{1}{2}} \mathcal{M}_{\alpha+\frac{1}{2}} - u_{\alpha-\frac{1}{2}} \mathcal{M}_{\alpha-\frac{1}{2}}, \quad (8)$$

where the mass exchange terms  $\mathcal{M}_{\alpha-\frac{1}{2}}$  and  $\mathcal{M}_{\alpha+\frac{1}{2}}$  are evaluated using

$$\mathcal{M}_{\alpha-\frac{1}{2}} = \begin{cases} 0, & \alpha = 1, \\ \sum_{i=1}^{\alpha} \left( \frac{\partial (h_i u_i)}{\partial x} - l_i \sum_{j=1}^N \frac{\partial (h_j u_j)}{\partial x} \right), & \alpha = 2, 3, \dots, N, \end{cases} \quad (9)$$

and

$$\mathcal{M}_{\alpha+\frac{1}{2}} = \begin{cases} \sum_{i=1}^{\alpha} \left( \frac{\partial (h_i u_i)}{\partial x} - l_i \sum_{j=1}^N \frac{\partial (h_j u_j)}{\partial x} \right), & \alpha = 1, 2, \dots, N-1, \\ 0, & \alpha = N, \end{cases} \quad (10)$$

respectively. Here, the interface velocities  $u_{\alpha-\frac{1}{2}}$  and  $u_{\alpha+\frac{1}{2}}$  are computed according to the sign of mass-exchange terms in (9) and (10) as

$$u_{\alpha-\frac{1}{2}} = \begin{cases} u_{\alpha-1}, & \mathcal{M}_{\alpha-\frac{1}{2}} \geq 0, \\ u_\alpha, & \mathcal{M}_{\alpha-\frac{1}{2}} < 0, \end{cases} \quad u_{\alpha+\frac{1}{2}} = \begin{cases} u_\alpha, & \mathcal{M}_{\alpha+\frac{1}{2}} \geq 0, \\ u_{\alpha+1}, & \mathcal{M}_{\alpha+\frac{1}{2}} < 0. \end{cases} \quad (11)$$

Note that a zeroth-order approximation of the  $2(M-1)$  barotropic eigenvalues associated with  $(M-1)$  interfaces gives

$$\lambda_{int}^{\pm, \alpha+\frac{1}{2}} = v \pm \sqrt{\frac{1}{2} g \sum_{\alpha=1}^M h_\alpha + \mathcal{O}(|v_\beta - v|)_{\beta=1, \dots, M}}, \quad \alpha = 1, 2, \dots, M-1. \quad (12)$$

### 3 Hybrid finite element/finite volume solver

To solve the above system we consider a finite element method for the two-dimensional elasticity equations. The starting point for the finite element method is the domain discretization. In the present study, we adopt the finite element method proposed in [1] using an unstructured mesh with quadratic triangular elements. Hence, the variational formulation of (1)-(2) consists of forming the inner product of equation (1) by a vector test function  $\phi$  and integrate over the domain  $\Omega$

$$\int_{\Omega} (\nabla \cdot \boldsymbol{\sigma}) \cdot \phi \, d\mathbf{x} = \int_{\Omega} \mathbf{f} \cdot \phi \, d\mathbf{x}, \quad (13)$$

where  $\mathbf{x} = (x, z)^\top$  and  $\mathbf{n} = (n_x, n_z)^\top$  is the outward unit normal on  $\partial\Omega$ . Integrating the system by parts, since  $\nabla \cdot \boldsymbol{\sigma}$  contains second-order derivatives of the primary unknown  $u$

$$\int_{\Omega} (\nabla \cdot \boldsymbol{\sigma}) \cdot \phi \, d\mathbf{x} = \int_{\Omega} \boldsymbol{\sigma} : \nabla \phi \, d\mathbf{x} - \oint_{\partial\Omega} (\boldsymbol{\sigma} \cdot \mathbf{n} \cdot \phi) \, ds, \quad (14)$$

where the colon operator is the inner product between tensors (summed pairwise product of all elements). Here,  $\boldsymbol{\sigma} \cdot \mathbf{n}$  is the traction or stress vector at the boundary, and is often prescribed as a boundary condition. Using that the traction stress vector  $\mathbf{T} = \boldsymbol{\sigma} \cdot \mathbf{n}$ , thus we obtain

$$\int_{\Omega} \boldsymbol{\sigma} \cdot \nabla \phi \, d\mathbf{x} = \int_{\Omega} \mathbf{f} \cdot \phi \, d\mathbf{x} + \oint_{\partial\Omega} \mathbf{T} \cdot \phi \, d\mathbf{x}, \quad (15)$$

which can be reformulated in a vector form as

$$\int_{\Omega} \hat{\phi} \cdot \boldsymbol{\sigma} \, d\mathbf{x} = \oint_{\Omega} \phi^\top \cdot \mathbf{T} \, d\mathbf{x} + \int_{\Omega} \phi^\top \cdot \mathbf{f} \, d\mathbf{x}, \quad (16)$$

where  $\phi = (\phi_x, \phi_z)^\top$ ,  $\mathbf{T} = (\mathbf{T}_x, \mathbf{T}_z)^\top$  and  $\hat{\phi} = \left( \frac{\partial \phi_x}{\partial x}, \frac{\partial \phi_z}{\partial z}, \frac{\partial \phi_x}{\partial z} + \frac{\partial \phi_z}{\partial x} \right)^\top$ . To solve the weak form (16) with the finite element method, the domain  $\Omega$  is discretized into a set of elements where the solution is approximated in terms of the nodal values  $U_j$  and the polynomial basis functions  $\Psi_j(x, z)$  as

$$\mathbf{u}(x, z) = \sum_{j=1}^N \mathbf{U}_j \Psi_j(x, z), \quad (17)$$

where  $N$  is the number of nodes. To solve the fully discretized problem, the elementary matrices are assembled into a global system of equations

$$\mathbf{K}\mathbf{u} = \mathbf{f}, \quad (18)$$

where  $\mathbf{K}$  is the global stiffness matrix,  $\mathbf{u}$  is the nodal displacement vector and  $\mathbf{f}$  is the force vector.

Next, the multi-layer shallow water system with mass exchange was implemented for the water perturbations. For the spatial discretization of (6), we discretise the spatial domain into control volumes  $[x_{i-1/2}, x_{i+1/2}]$  with uniform size  $\Delta x = x_{i+1/2} - x_{i-1/2}$ ,  $x_{i-1/2} = i\Delta x$  and  $x_i = (i + 1/2)\Delta x$  is the center of the control volume. Integrating the equation (6) with respect to space over the control volume  $[x_{i-1/2}, x_{i+1/2}]$ , we obtain the following semi-discrete equations

$$\frac{d\mathbf{W}_i}{dt} + \frac{\mathcal{F}_{i+1/2} - \mathcal{F}_{i-1/2}}{\Delta x} = \mathbf{Q}(\mathbf{W}_i) + \mathbf{R}(\mathbf{W}_i), \quad (19)$$

where  $\mathbf{W}_i(t)$  is the space-averaged approximation of the solution  $\mathbf{W}$  in the control volume  $[x_{i-1/2}, x_{i+1/2}]$  at time  $t$ , *i.e.*,

$$\mathbf{W}_i(t) = \frac{1}{\Delta x} \int_{x_{i-1/2}}^{x_{i+1/2}} \mathbf{W}(t, x) dx,$$

and  $\mathcal{F}_{i\pm 1/2} = \mathbf{F}(\mathbf{W}_{i\pm 1/2})$  are the numerical fluxes at  $x = x_{i\pm 1/2}$  and time  $t$ . Here, the time integration of (19) is performed using a second-order splitting method studied in [19]. Thus, to integrate the equations (6) in time we divide the time interval into subintervals  $[t_n, t_{n+1}]$  with length  $\Delta t = t_{n+1} - t_n$  for  $n = 0, 1, \dots$ . We also use the notation  $W^n$  to denote the value of a generic function  $W$  at time  $t_n$ . The considered operator splitting method consists of three stages as presented in [2]. The spatial discretization (19) is complete when a reconstruction of the numerical fluxes  $\mathcal{F}_{i\pm 1/2}$  and source terms  $\mathbf{Q}(\mathbf{W}_i)$  and  $\mathbf{R}(\mathbf{W}_i)$  are chosen. In the current work, the finite volume method of characteristics studied in [5] has been implemented and it can be rearranged in a compact form as

$$\frac{\partial U_\alpha}{\partial t} + U_\alpha \frac{\partial U_\alpha}{\partial x} = S_\alpha(\mathbf{U}), \quad \alpha = 0, 1, \dots, M, \quad (20)$$

where  $q_\alpha = H v_\alpha$  is the water discharge,  $\mathbf{U} = (U_0, U_1, \dots, U_M)^T$ ,  $\mathbf{S}(\mathbf{U}) = (S_0, S_1, \dots, S_M)^T$  with

$$\mathbf{U} = \begin{pmatrix} H \\ q_1 \\ q_2 \\ \vdots \\ q_M \end{pmatrix}, \quad \mathbf{S}(\mathbf{U}) = \begin{pmatrix} -\sum_{\alpha=1}^M l_\alpha H \frac{\partial v_\alpha}{\partial x} \\ -H v_1 \frac{\partial v_1}{\partial x} - gH \frac{\partial}{\partial x} (H + Z) \\ -H v_2 \frac{\partial v_2}{\partial x} - gH \frac{\partial}{\partial x} (H + Z) \\ \vdots \\ -H v_M \frac{\partial v_M}{\partial x} - gH \frac{\partial}{\partial x} (H + Z) \end{pmatrix},$$

and the advection velocity  $U_\alpha$  is defined as

$$U_\alpha = \begin{cases} \sum_{\beta=1}^M l_\beta v_\beta, & \text{if } \alpha = 0, \\ v_\alpha, & \text{if } \alpha = 1, 2, \dots, M. \end{cases} \quad (21)$$

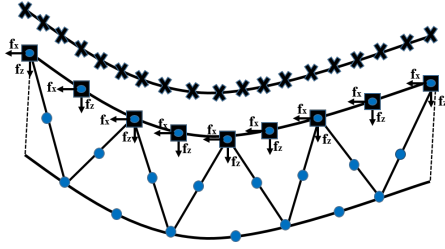


Fig. 2: Illustration of the finite element and finite volume nodes used for coupling conditions at the interface.

The characteristic curves associated with the equation (20) are solutions of the initial-value problems

$$\begin{aligned} \frac{dX_{\alpha,i+1/2}(\tau)}{d\tau} &= \mathcal{U}_{\alpha,i+1/2}(\tau, X_{\alpha,i+1/2}(\tau)), \quad \tau \in [t_n, t_{n+1}], \\ X_{\alpha,i+1/2}(t_{n+1}) &= x_{i+1/2}, \quad \alpha = 0, 1, \dots, M. \end{aligned} \quad (22)$$

where  $X_{\alpha,i+1/2}(\tau)$  are the departure points at time  $\tau$  of a particle that will arrive at the gridpoint  $x_{i+1/2}$  in time  $t_{n+1}$ . In our simulations we used the third-order Runge-Kutta method for the solution of the initial-value problems (22).

### 3.1 Coupling conditions at the interface

For the proposed model, coupling conditions are required to be transferred on the interface  $\Gamma$  at each time step between both the multi-layer and elasticity models. As illustrated in Figure 1, the finite element and finite volume nodes on the interface do not coincide in general and therefore we employ a cubic spline interpolation to interchange the solutions between the two classes of nodes. At each time step, coupling conditions are required on the interface to transfer information between both models. In the present work, the deformed finite element nodes on the interface are used to reconstruct the bed  $Z$  for the shallow water equations (6). This bed profile is used in the finite volume solution of the flow system to obtain the water depth  $h^{n+1}$  and the water velocity  $v^{n+1}$ . On the interface, the horizontal  $x$ -direction and vertical  $z$ -direction forces are sampled from the water flow. Here, at each time step, the finite volume solutions of the multi-layer model are used to calculate the hydrostatic pressure and the friction distributions. These are then used to sample the horizontal and vertical forces at the interface to be used in the finite element solutions of the elasticity model. Thus, the horizontal force  $f_x$  in the  $x$ -direction is calculated using the friction term as

$$f_x = -gn_b^2 \frac{v^{n+1} |v^{n+1}|}{(h^{n+1})^{\frac{1}{3}}}. \quad (23)$$

**Algorithm 1** Hybrid finite element/finite volume method.**Require:**  $E, \nu, \rho_w, n_b, h, u, C_r, T$ .

- 1: Assemble the stiffness matrix  $\mathbf{K}$  for the elastostatic system using the finite element method (16).
- 2: Assemble the force vector  $\mathbf{f}$  for the elastostatic system using the finite element method (1)-(2).
- 3: Solve the linear system (16) for the displacement in the computational mesh.
- 4: Solve the linear system (2) for the elastic strain in the computational mesh.
- 5: Solve the linear system (5) for the stresses distributions in the computational mesh.
- 6: Update the displacement of the finite element nodes on the interface.
- 7: Solve the shallow water equations using:
- 8: **for** each control volume  $[x_i, x_{i+\frac{1}{2}}]$  **do**
- 9:   Compute the numerical fluxes  $\mathbf{F}_{i\pm\frac{1}{2}}^n$ .
- 10:   Discretize the source term  $\mathbf{Q}_i$  using the well-balanced discretization.
- 11:   Compute the solution in the first stage of the splitting  $\mathbf{W}_i^{n+1}$ .
- 12:   Compute the solution in the second and third stages of the splitting  $\mathbf{W}_i^{n+1}$ .
- 13: **end for**
- 14: Compute the horizontal force  $f_x$  using the bed friction according to (23).
- 15: Compute the vertical force  $f_z$  using the hydrostatic pressure according to (24).
- 16: Update the time step  $\Delta t$  according to the CFL condition (26).
- 17: Overwrite  $t_n \leftarrow t_n + \Delta t$  and go to step 2.

Similarly, the vertical force  $f_z$  in the  $z$ -direction is computed at each time step using the variation in the hydrostatic pressure as

$$p^{n+1} = -\rho g \frac{h^{n+1} - h^n}{\Delta t_n}. \quad (24)$$

Therefore, the vertical force  $f_z$  at each node on the interface  $\Gamma$  is reconstructed using the integral form as [15]

$$\begin{aligned} f_z^{(1)} &= \int_{-1}^1 -\frac{1}{2}\xi(1-\xi)p^{n+1}\frac{\bar{h}}{2}d\xi \approx \frac{\bar{h}}{6}p^{n+1}, \\ f_z^{(2)} &= \int_{-1}^1 (1-\xi^2)p^{n+1}\frac{\bar{h}}{2}d\xi \approx \frac{2\bar{h}}{3}p^{n+1}, \\ f_z^{(3)} &= \int_{-1}^1 \frac{1}{2}\xi(1+\xi)p^{n+1}\frac{\bar{h}}{2}d\xi \approx \frac{\bar{h}}{6}p^{n+1}, \end{aligned} \quad (25)$$

where  $\bar{h}$  is the length of the edge in the considered triangular element on the interface. Hence, once the element forces  $f_z^{(1)}$ ,  $f_z^{(2)}$  and  $f_z^{(3)}$  are calculated according to (25), the global force  $f_z$  to be applied in the  $z$ -direction is calculated by accumulating the elemental forces on the overlapped nodes. Note that it is easy to verify that the element forces (25) satisfy the relation

$$f_z^{(1)} + f_z^{(2)} + f_z^{(3)} = \bar{h}p^{n+1}.$$

In present work, we refer to our approach as fully coupled, because at each time step the solution of the finite volume method depends on the solution of finite element method and vice versa. While the discretized systems are not assembled into a monolithic system, the coupling is achieved through mutual dependencies between these separate solvers, these steps are described in Algorithm 1.

## 4 Computational results

The main goals of this section are to illustrate the numerical performance of the techniques prescribed in the previous sections and verify numerically their capability to capture the wind circulation and accurately calculate the stresses induced in the deformable beds. In all the computations reported herein, the Courant number is set to  $Cr = 0.7$  and the timestep size  $\Delta t$  is adjusted at each time step according to the following CFL stability condition

$$\Delta t = Cr \frac{\Delta x}{\max_{\alpha=1,\dots,M} (|\lambda_{\alpha}^n|)}, \quad (26)$$

where  $M$  is the number of layers, and  $\lambda_{\alpha}^n$  is the corresponding eigenvalues in each layer given in (12).

### 4.1 Accuracy results

In this example, we investigate the accuracy of techniques proposed in the present work. Firstly, we examine the performance of the considered multi-layer finite volume method to the analytical solution of the wind flow problem over a flat bed presented in [17]. To this end, the velocity of 5, 10, 20 and 50 layers free-surface over a flat bed (*i.e.*  $Z = 0$ ) with 3400  $m$  length and 10  $m$  height are compared to the analytical solutions. The domain is divided into 100 control volumes and the following parameters were implemented: the air density,  $\rho_a = 1.2 \text{ kg/m}^3$ , water density  $\rho = 1025 \text{ kg/m}^3$ , friction coefficient  $k = 0.1 \text{ m/s}$ , wind stress coefficient  $\sigma^2 = 0.0015$ , viscosity coefficient  $\xi = 0.1 \text{ m}^2/\text{s}$  and acceleration of gravity  $g = 9.81 \text{ m/s}^2$ . Figure 3a exhibits the velocity profile obtained at time  $t = 1000 \text{ s}$  compared to the analytical solution. A good agreement between the numerical and analytical solutions are shown in this figure. The convergence to the analytical solution can be clearly seen as the number of layers increases.

For a numerical validation of the finite element method, the model presented in [16] has been compared to our finite element numerical solution. In this model, a squared plate foot is used in the test with a width of  $R = L = 150 \text{ mm}$  and thickness of 20  $mm$ . A vertical stress of  $47 \text{ KN/m}^2$  is implemented at the center of the squared domain. In this example, a finite element linear elastic model with Young's modulus  $E = 28000 \text{ KN/m}^2$  and Poisson's ratio  $\nu = 0.20$  is implemented. A comparison between the numerical and experimental vertical stresses at different points is shown in Figure 3b. It can be seen that experimental results are in good agreement with numerical results. Under the considered elasticity condition, it has been found that the difference between the analytical and numerical results is only 6.5%.

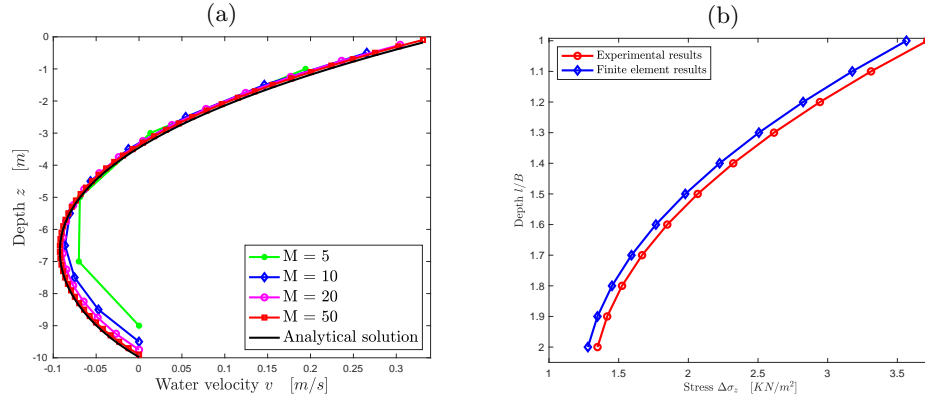


Fig. 3: Accuracy results for the finite volume method solving the multi-layer flow problem (a) and accuracy results for the finite element method solving the elastostatic bed problem (b).

#### 4.2 Wind-driven circulation flow by pipe failure in the topography

The problem of pipe failures are among the common examples that received attention from civil and geotechnical engineers, see for example [7]. In these failures, the source of deformation comes from below the seabed surface. In this example, we consider shallow water waves generated by failure of two pipes in the bed topography. A rectangular domain 50 m long and 7 m high including two circular pipes with radius  $R = 2.1$  m each and the initial water height is 5 m above the bed. A compressive force of 200 N is applied only at the upper half boundary of the pipes. Initially, the system is at rest and at time  $t = 50$  s the constant force is applied on the upper surface of the pipes. Consequently, a deformation is expected on the pipes and therefore transmitted to the shallow water bed which generates water waves on the free-surface. The finite volume domain is discretized into 200 control volumes and the following parameters were implemented: the air density,  $\rho_a = 1.2$  kg/m<sup>3</sup>, water density  $\rho = 1000$  kg/m<sup>3</sup>, friction coefficient  $k = 1 \times 10^{-1}$  m/s, wind stress coefficient  $\sigma^2 = 0.0015$ , viscosity coefficient  $\xi = 0.01$  m<sup>2</sup>/s, wind speed 5 m/s, acceleration of gravity  $g = 9.81$  m/s<sup>2</sup>, modulus of elasticity  $E = 10000$  KN/m<sup>2</sup> and Poisson's ratio  $\nu = 0.3$ . A finite element mesh with 2471 elements and 5160 nodes is implemented in our simulations. In Figure 4, the velocity fields obtained at time steps  $t = 50$  s, 100 s and 120 s using 50 layers are presented. In this figure, the wind flows toward the right side of the domain leading to an initial water circulation with a vortex close to the right side of the domain. At a later time  $t = 100$  s, the bed deformation occurred causing the water to perturb and so the water flow field is directed toward the maximum deformation in the bed. This model accurately responds to the sudden bed deformation and captures the water perturbation without any oscillations on the surface. The finite element method represents the bed deformation without any mesh distortion and without the need for a very refined

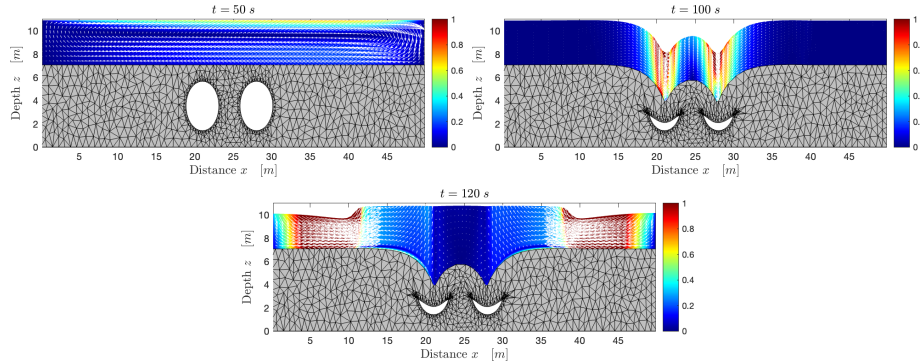


Fig. 4: Bed deformations and water velocity fields at three different times.

Table 1: Effects of wind speed and number of layers on the circulation centers.

| $t = 1000 \text{ s}, w = 5 \text{ m/s}$ |                       | $t = 1000 \text{ s}, 50 \text{ layers}$ |                       |
|---|-----------------------|---|-----------------------|
| Number of layers                        | Center of circulation | Wind speed                              | Center of circulation |
| $M = 50$                                | (38.75, 9.72)         | $5 \text{ m/s}$                         | (38.75, 9.72)         |
| $M = 30$                                | (42.25, 9.722)        | $10 \text{ m/s}$                        | (43.25, 9.723)        |
| $M = 20$                                | (43.25, 9.723)        | $15 \text{ m/s}$                        | (45.25, 9.724)        |
| $M = 10$                                | (43.55, 9.723)        | $20 \text{ m/s}$                        | (47.25, 9.886)        |

mesh in the domain. An upward reflected wave is detected at time  $t = 120 \text{ s}$ , the waves remain perturbed till they reach stability at time  $t = 1000 \text{ s}$ . As can be seen in these results, a central circulation has been generated in the flow channel due to these deformations in the bed. It is worth mentioning that these circulations cannot be captured using the single-layer shallow water models, we refer the reader to [1, 2] to compare the single-layer coupling results of this problem. It is clear that the center of this vortex is affected by the number of layers used in the computations and the wind speed. To further demonstrate this effect, centers of these recirculations using different numbers of layers and different wind speeds are summarised in Table 1. The center of the circulation is shifted to the right when the wind speed increases and when the number of layers decreases.

For further investigations, we presented in Figure 3 the velocity profiles at the location  $x = 40 \text{ m}$  obtained at time  $t = 1000 \text{ s}$ . We also include in this figure cross-sections results for the vertical stress  $\sigma_z$ , the horizontal stress  $\sigma_x$  and the shear stress  $\tau_{xz}$  at the location  $x = 40 \text{ m}$ . Here, we considered 10, 20, 30 and 50 layers. For comparison, we also include a reference velocity field obtained for the 50 layers model using a very fine mesh of 1200 control volumes. It can be clearly shown from this figure, that an increase of the number of layers in the model illustrate a perfect convergence to the reference solution. The model

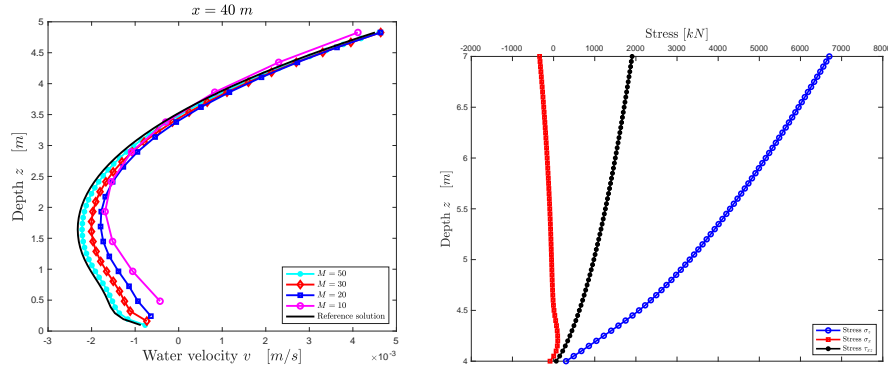


Fig. 5: Velocity profile at  $x = 40 \text{ m}$  using different layers (left) and cross-sections of the stresses at  $x = 40 \text{ m}$  (right).

also accurately captures the velocity flow using a different number of layers and without any spurious oscillations or excessive numerical diffusion.

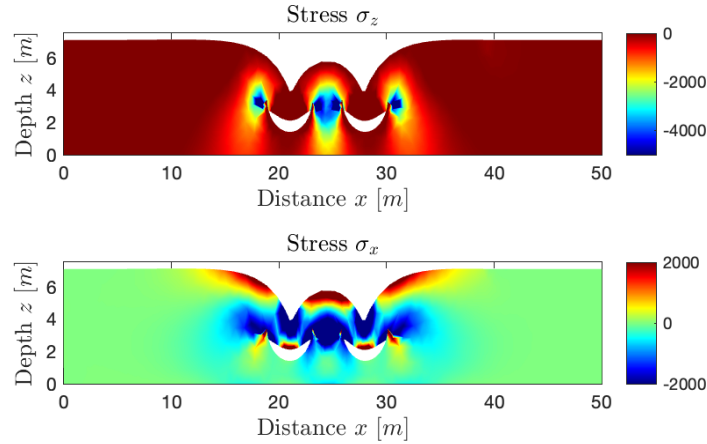


Fig. 6: Distribution for the stresses  $\sigma_z$  (top) and  $\sigma_x$  (bottom) obtained for shallow water waves generated by a pipe failure in the topography at time  $t = 50 \text{ s}$ .

To investigate the distributed stresses resulting from the pipes failure underground. The two main dialary stresses  $\sigma_z$  and  $\sigma_x$  are shown in Figure 6. It is clear from this figure that high stresses are distributed around the highest deformation in the bed. It is clear from these results that the stresses are distributed symmetrically around the vertical centerline of the mesh. The finite element method performs well and it reproduces stable solutions without non-

physical oscillations at stresses distributions. To examine the stress distributions with the bed depth, plots of vertical cross-sections in the stresses at the point  $x = 21 \text{ m}$  for the vertical stresses  $\sigma_z$ , horizontal stresses  $\sigma_x$  and the shear stress  $\tau_{xz}$  are presented in Figure 3. It can be noted from this figure that the vertical stresses have the highest values and the shear stresses are the lowest. It is also clear that the stress values are decreasing far from the location of the applied force and the maximum values are detected near the point of force effects.

## 5 Conclusions

A simple and accurate approach to couple free-surface multi-layer flows with bed deformations has been presented. The governing equations consist of coupling the nonlinear shallow water equations for water flow to the linear equations for elasticity. The coupling conditions between the two models is achieved through the interface between the two bodies and only the updated topography is required for the free-surface simulations. The hydrostatic pressure from water flow is also accounted for in the bed deformation and it is applied as external force on the elasticity model. As numerical solvers, we have considered a conservative finite volume method for the free-surface flow and a robust finite element method for the bed deformation. The new method has several advantages: First, it can solve steady flows over irregular beds without large numerical errors. Second, it can compute the numerical flux corresponding to the real state of water flow without relying on Riemann problem solvers. Third, reasonable accuracy can be obtained easily and no special treatment is needed to maintain a numerical balance, because it is performed automatically in the integrated numerical flux function. Furthermore, it has strong applicability to various problems in shallow water flows over deformed beds as shown in the numerical results. The proposed approach has been numerically examined for the test example of free-surface flow problems. The results make it promising to be applicable also to real situations where, beyond the many sources of complexity, there is a more severe demand for accuracy in predicting free-surface waves induced by sudden bed deformations, which must be performed for a long time. Future research will focus on the extension of these techniques to nonlinear plasticity in the bed deformation to allow strong interactions of water flows on largely deformed soils.

## References

1. Al-Ghosoun, A., Osman, A., Seaid, M.: A hybrid finite volume/finite element method for shallow water waves by static deformation on seabeds. *Engineering Computations* **38**, 2434–2459 (2021)
2. Al-Ghosoun, A., Osman, A.S., Seaid, M.: A computational model for simulation of shallow water waves by elastic deformations in the topography. *Communications in computational physics*. **29**, 1095–1124 (2021)
3. Alongi, F., Puma, D., Nasello, C., Nizzo, S., Ciraolo, G., Noto, L.: An automatic ANN-based procedure for detecting optimal image sequences supporting LS-PIV applications for rivers monitoring. *Journal of hydrology* **626**, 130–167 (2023)

4. Audusse, A.: A multilayer Saint Venant system: Derivation and numerical validation. *Discrete and continuous dynamical systems* **5**, 189–214 (2005)
5. Benkhaldoun, F., Sari, S., Seaid, M.: A simple multi-layer finite volume solver for density driven shallow water flows. *Mathematics and computers in simulation* **99**, 170–189 (2014)
6. Duan, Q.: On the dynamics of Navier-Stokes equations for shallow water model. *Journal of differential equations* **250**, 2687–2714 (2011)
7. Gao, F., Jeng, D., Sekiguchi, H.: Numerical study on the interaction between nonlinear wave, buried pipe line and non-homogenous porous seabed. *Computers and Geotechnics* **30**, 535–547 (2003)
8. Higdon, R.: An automatically well-balanced formulation of pressure forcing for discontinuous Galerkin methods for the shallow water equations. *Journal of computational physics* **458**, 205–221 (2022)
9. Holtz, R., Kovacs, W., Sheahan, T.: Introduction to geotechnical engineering. *Journal of hydraulic engineering* **130**, 689–703 (2004)
10. Huang, J., Xie, X., Gao, Y., Xu, S., Zhu, M., Hu, Z., Xu, P.: Multi-layer flow field mapping in a small-scale shallow water reservoir by coastal acoustic tomography. *Journal of hydrology* **617**, 233–265 (2023)
11. Izem, N., Seaid, M.: A well-balanced Runge-Kutta discontinuous Galerkin method for multi-layer shallow water equations with non-flat bottom topography. *Advances in applied mathematics and mechanics* **14**, 725–758 (2022)
12. Liu, P., Wang, X.: A multi-layer model for nonlinear internal wave propagation in shallow water. *Journal of fluid mechanics* **695**, 341–365 (2012)
13. Ortega, E., Onate, E., Idelsohn, S.: Method for shallow water equations. *International Journal for numerical methods in engineering* **88**, 180–204 (2011)
14. Ran, Q., Tong, J., Shao, S., Fu, X., Xu, Y.: Incompressible SPH scour model for movable bed dam break flows. *Advances in water resources* **82**, 39–50 (2015)
15. Sairajan, K., Deshpande, S., Patnaik, M., Poomani, D.: Base force and moment based finite element model correlation method. *Advances in space research* **68**, 4056–4068 (2021)
16. Saleh, M., Laman, M., Baran, T.: Experimental determination and numerical analysis of vertical stresses under square footings resting on sand. *Digest* **19**, 4521–4538 (2008)
17. Shankar, N., Cheong, H., Sankaranarayanan, S.: Multilevel finite-difference model for three-dimensional hydrodynamic circulation. *Ocean engineering* **24**, 785–816 (1997)
18. Stewart, A., Dellar, P.: An energy and potential enstrophy conserving numerical scheme for the multi-layer shallow water equations with completer Coriolis force. *Journal of computational physics* **313**, 99–120 (2016)
19. Strang, G.: On the construction and the comparison of difference schemes. *SIAM J. Numer. Anal* **5**, 506–517 (1968)
20. Teja, K., Manikanta, V., Das, J., Umamahesh, N.: Enhancing the predictability of flood forecast by combining numerical weather prediction ensembles with multiple hydrological models. *Journal of hydrology* **625**, 130–167 (2023)
21. Tubbas, K., Tsai, F.: Multilayer shallow water flow using lattice Boltzmann method with high performance computing. *Advances in water resources* **32**, 1767–1776 (2009)
22. Zhang, Z., Tang, H., Duan, J.: High-order accurate well-balanced energy stable finite difference scheme for multi-layer shallow water equations on fixed and adaptive moving meshes. *Journal of hydrology* **617**, 811–823 (2023)